Available online at www.sciencedirect.com
ScienceDirect
Trans. Nonferrous Met. Soc. China 34(2024) 3554−3568
Transactions of Nonferrous Metals Society of China
www.tnmsc.cn

Synergistic effect of orientation and temperature on slip behavior and precipitation behavior of Al−Cu−Li single crystals

Zhen JIANG[1], Chen-qi LEI[1], Jia-jun DING[1], Chun-nan ZHU[1], Dong-feng SHI[1,2], Jin ZHANG[1,2], Guo-qing WANG[3]

1. Light Alloy Research Institute, Central South University, Changsha 410083, China;
2. State Key Laboratory of High Performance and Complex Manufacturing, Central South University, Changsha 410083, China;
3. China Academy of Launch Vehicle Technology, Beijing 100076, China

Received 30 June 2024; accepted 8 October 2024

Abstract: The slip behavior and precipitation behavior of four Al−Cu−Li single crystals with varying orientations at different temperatures were investigated using electron backscattering diffraction (EBSD) and transmission electron microscopy (TEM). The maximum differences in yield strength and ductility of the single crystals at room temperature are 41.6% and 14.7%, respectively. This indicates that the mechanical properties are strongly influenced by the crystal orientation. Moreover, grains with varying orientations exhibit distinct slip characteristics, including slip homogenization, slip localization, and multiple slip. In single crystal SC1, slip localization primarily contributes to its inferior ductility compared to other grains. Nevertheless, during deformation at 250 °C, the distinct morphology and distribution of precipitates in the crystals are also correlated with orientation, which causes the increase in the maximum elongation difference to 20.8% in all selected single crystals. Notably, SC1, with a precipitate volume fraction of 2.65%, exhibits more severe slip localization compared to room temperature conditions, while SC2, with a precipitate volume fraction of 4.79%, demonstrates cross-slip characteristics, significantly enhancing the plastic deformation capacity of the Al−Cu−Li alloy.

Key words: Al−Cu−Li alloy; single crystal; slip behavior; oriented precipitation; deformation mechanism

1 Introduction

Al−Cu−Li alloys have excellent properties such as low density, high strength and high modulus, thus garnering considerable attention in aerospace, automobile manufacturing, and other industries [1]. However, the Al−Cu−Li alloy sheets exhibit pronounced mechanical anisotropy, significantly impacting forming accuracy and service life [2]. Texture and precipitates play crucial roles in the anisotropy of Al−Cu−Li alloys. During the deformation process of Al−Cu−Li alloy, a brass texture is easily formed, notably enhancing sheet metal anisotropy [3]. Moreover, a higher volume fraction of brass components exacerbates plate anisotropy [4]. The 2024 alloy, with conventional rolling, exhibits the highest ductility along the rolling direction, while the anisotropy is reduced with constrained groove pressing after two passes [5]. NAYAN et al [6] found that the strong brass texture formed in the cross rolled 2195 Al−Li alloy is weakened after subsequent heat treatment, resulting in a transition from anisotropic to isotropic properties of the material.

$T1$ (Al_2CuLi) and θ'(Al_2Cu) phases serve as the primary strengthening phases of Al−Cu−Li alloys. $T1$ phase is precipitated on {111} surface of

Corresponding author: Dong-feng SHI, Tel: +86-18569483690, E-mail: dongfeng.shi@csu.edu.cn
DOI: 10.1016/S1003-6326(24)66625-2

the matrix, which is also the slip surface of the Al−Cu−Li alloy [7]. Pre-deformation treatment introduces numerous dislocations in the matrix, enhancing precipitate nucleation density and facilitating the adjustment of the distribution and size of θ' and $T1$ phases, thereby improving mechanical properties [8,9]. The precipitation of $T1$ phase is directly linked to dislocation density, with uniform dislocation distribution promoting homogeneous $T1$ phase dispersion throughout the matrix, resulting in superior mechanical properties [10−12]. However, some orientations exhibit a higher average precipitation strengthening factor of $T1$ phase, potentially intensifying the strength anisotropy of alloy [13]. MEDJAHED et al [14] observed significant differences in the distribution of precipitates in Al−Cu−Li sheet after cold rolling in different directions, resulting in different mechanical anisotropy. The θ' phase, with the magnitude of adjustable strain determined by the crystal orientation of these grains, can adjust the strain of the surrounding matrix through rotation, and varying distributions of the θ' phase lead to orientation-dependent strain hardening [15]. Different proportions of the $T1$ and θ' phases result in distinct deformation mechanisms during the plastic deformation of the alloy, consequently impacting its properties [16]. The distribution of $T1$ on four different {111} planes is jointly determined by texture and pre-deformation, thereby influencing the yield strength anisotropy of alloys subjected to different pre-deformation treatments [17]. A framework for calculating anisotropic yield strength based on the VPSC model was established [18]. It revealed significant differences in the volume fraction of the four variants of the $T1$ phase after pre-deformation in different directions, leading to changes in the critical resolved shear stress (CRSS) of each slip system and ultimately resulting in varying levels of anisotropy. LIU et al [19,20] established a crystal plastic model by finite element method, considered plastic slip and lattice rotation as the deformation mechanism, to study the anisotropic stacking behavior of single crystal copper with different initial orientations during nanoindenting. They found that the activation of different slip systems had a certain effect on the anisotropy of the stacking mode. Although there are many studies on the effect of orientation on the precipitated phase, most simulated this process using crystal plastic finite element methods, lacking accurate experimental data.

The slip direction and slip plane orientation of the dislocation will affect the plastic deformation behavior of the material in different directions, which can be reflected on the specimen surface. The deformation mechanisms of the material during plastic deformation can be analyzed by statistical analysis of the grain surface slip traces. The method was widely employed in studying the plastic deformation of materials [21−23]. In polycrystalline materials, texture represents the preferred orientation structure of grains. When studying the influence of texture on anisotropy, the existence of grain boundaries increases the diversity of deformation mechanisms, making it challenging to accurately analyze the influence of single crystal orientation on precipitation, deformation behavior, and anisotropy [24−27].

Hence, in this work, the effect of orientation on the mechanical properties and slip behavior of four Al−Cu−Li single crystals with varying orientations through uniaxial stretching at different temperatures was investigated. Additionally, the impact of orientation on dynamic precipitation during high-temperature deformation was examined. Importantly, the influence of oriented-precipitation on the deformation mechanism was discussed.

2 Experimental

The material employed in this study is an Al−4Cu−1Li (wt.%) ternary alloy. It was cast by vacuum melting and homogenized for 20 h at 500 °C. The Al−Cu−Li alloy ingot was rolled into 10 mm-thick sheets at 460 °C. The rolled sheet was cut into 140 mm × 40 mm blocks, the block sample was stretched with small deformation, and then annealed at 510 °C for 24 h. The ultra-large grains with a size of 3.2 cm were prepared by cyclic deformation−annealing process, as shown in Fig. 1(a). The samples for tensile testing, measuring 22 mm in length, 10 mm in width, and 2 mm in thickness, were prepared in a single grain by means of electrical discharge machining, as shown in Figs. 1(b, c). Each specimen is a single crystal.

Different regions of the standard orientation triangle can approximately reflect the dislocation slip mode, as shown in Fig. 2(a), which includes the single slip, double slip, coplanar double slip,

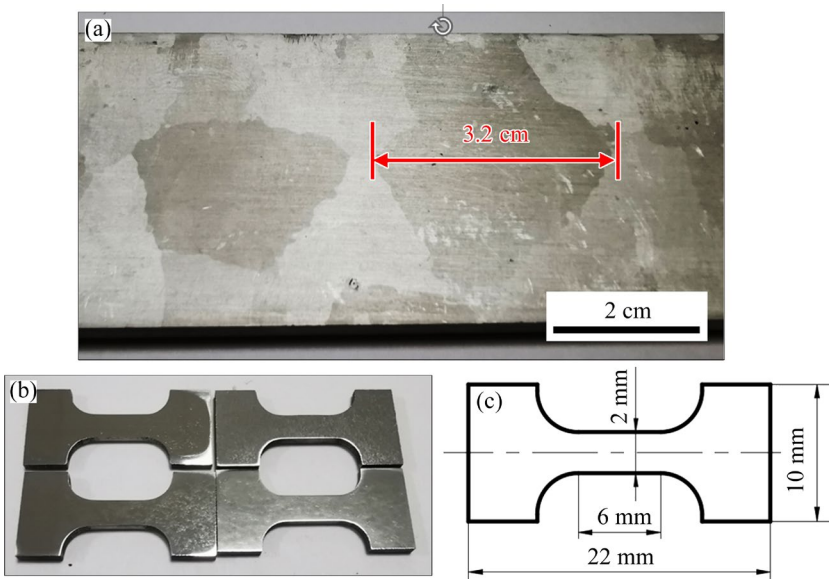

Fig. 1 Ultra-large grain specimen of Al−Cu−Li alloy (a); Drawing of tensile specimens (b); Dimensions of tensile specimen with thickness of 2 mm (c)

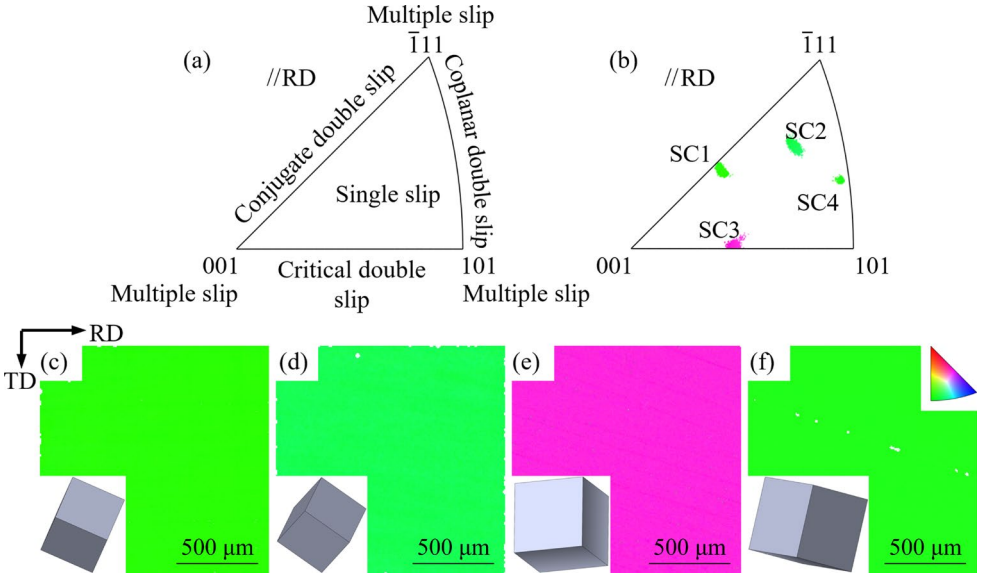

Fig. 2 Crystallographic triangle showing orientations of different slip modes [29] (a); Inverse pole figures (IPF) showing orientation of single crystals (b); EBSD IPF maps of single crystals of SC1 (c), SC2 (d), SC3 (e) and SC4 (f)

conjugate double slip and critical double slip [28]. With TESCAN Mira4 scanning electron microscope, the crystallographic orientations of the single crystal samples were observed by electron backscattering diffraction (EBSD), and grains with four orientations were selected according to Fig. 2(a), as shown in Figs. 2(b−f). These grains are oriented along the rolling direction (RD), approximately $[\bar{3}\bar{1}1]$, $[3\bar{4}\bar{2}]$, $[03\bar{1}]$ and $[\bar{3}\bar{1}3]$, respectively, labeled as SC1, SC2, SC3, and SC4. The tensile loading direction aligns parallel to the RD. The surface microstructure and fracture morphology of single crystal specimens during tensile deformation were observed via scanning electron microscopy (SEM). To minimize damage from the electron beam to the specimen surface, the corresponding beam current was reduced to 5 nA and 300 pA, respectively, during EBSD and SEM analysis. Subsequently, the EBSD data were analyzed using AztecCrystal software. Slip systems and Schmid factors of single crystals with different orientations were calculated and analyzed using the MATLAB toolbox MTEX. Slip trace analysis was performed using ImageJ software. The precipitation

behavior during high-temperature stretching was characterized using transmission electron microscopy (TEM) (Talos F200X).

The tensile samples were continuously polished with 9, 3, and 1 μm diamond polishing paste, and finally polished with silicon medium paste. First, TEM specimens were mechanically thinned to a thickness of 80 μm, followed by cutting them into discs with a diameter of 3 mm. A Tenupol Type 5 machine was then used to electropolish the flakes at −25 °C in a solution consisting of 20% nitric acid and 80% methanol. The tensile samples were solution treated at 500 °C for 60 min before stretching. A CMT5105GL testing machine was used for the tensile test, and the tensile speed was set at 0.2 mm/min. The high-temperature drawing process was insulated by a heating device. At least three samples were tested under the same conditions to ensure the accuracy of the data.

3 Results

3.1 Tensile results

The mechanical properties of Al−Cu−Li single crystals at room temperature and 250 °C are depicted in Fig. 3. At room temperature, strong orientation dependence of mechanical properties is illustrated in Fig. 3(a). The maximum differences in yield strength and elongation are observed to be 41.6% and 18.3%, respectively. SC4 exhibits significantly higher yield strength compared to the other single crystals. In contrast, the variation in tensile strength is minimal, with the largest difference being only 9.1%. Upon increasing the tensile temperature to 250 °C, the difference in yield strength among single crystals with different orientations decreases to 20.1%, as shown in Fig. 3(b). However, the maximum differences in tensile strength and elongation at 250 °C increase to 17.9% and 32.6%, respectively. This indicates substantial differences in the orientation-dependent properties of Al−Cu−Li at different temperatures. Additionally, as depicted in Fig. 3(c, d), the overall mechanical properties of Al−Cu−Li single crystals at 250 °C exhibit a decline relative to those at room temperature. The decline is attributed to the reduced CRSS of the slip system at 250 °C, resulting in a monotonic decrease with increasing temperature [30]. Furthermore, a detailed examination of the high-temperature stress−strain curve reveals an interesting phenomenon (Fig. 3(b)). Although work

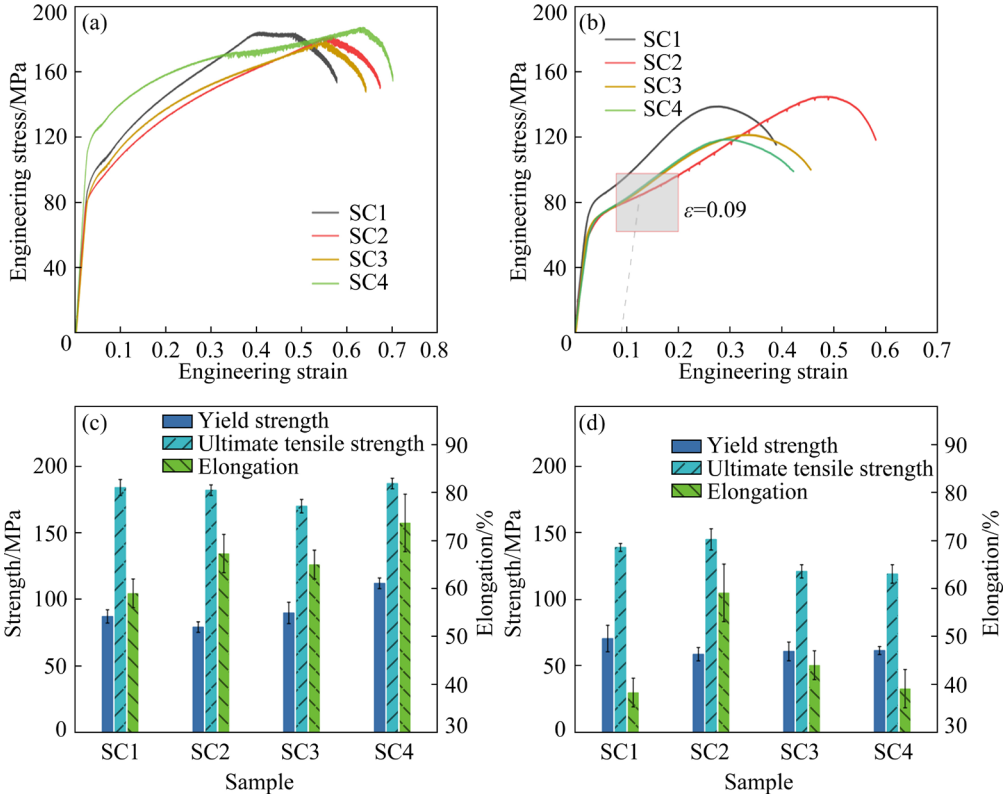

Fig. 3 Tensile engineering stress−strain curves (a, b) and tensile properties (c, d) at room temperature (a, c) and 250 °C (b, d)

hardening typically prevails, an upward opening segment is observed in the early stages of tensile deformation. This is attributed to the rapid decline in the work hardening rate induced by dynamic recovery. With the accumulation of strain, the disparity between the dislocation multiplication rate and the dynamic softening rate progressively widens, leading to a downward turn on the curve.

3.2 Slip activity

In the process of deformation, the activation of slip systems plays a considerable role in determining the plastic deformation behavior of material. The likelihood of slip system activity can be predicted by calculating the Schmid factor. The Schmid factors of 12 slip systems for the four orientations of the single crystals in this study are given in Table 1.

To determine the potential slip systems activated within each grain, detailed observations were made on the SEM images of the deformed specimens to analyze the consistency between the observed slip traces within each grain and the calculated results. The slip traces resulting from 15% tensile strain of single crystals at room temperature are illustrated in Fig. 4. Slip traces refer to the lines formed after dislocations move from the slip plane to the sample surface. Different colors in this figure correspond to different slip planes, and $(\bar{1}1\bar{1})$, $(\bar{1}11)$, (111) and $(\bar{1}\bar{1}1)$ planes are represented by red, blue, green and yellow, respectively. By comparing the software calculation results with the slip traces measured by SEM, the active slip planes are determined and displayed in the lattice cell (Fig. 4). Due to the large lattice rotation during deformation, the observed slip trace directions are slightly different from the calculated ones. Then, the main slip system and the secondary slip system are determined by the calculation results of the Schmid factor in Table 1.

Table 1 Schmid factors of 12 slip systems

Slip system	Plane	Direction	Schmid factor			
			SC1	SC2	SC3	SC4
1	$(\bar{1}1\bar{1})$	[011]	0.24	0.31	0.22	0.06
2	$(\bar{1}1\bar{1})$	[110]	0.22	0.11	0.30	0.11
3	$(\bar{1}1\bar{1})$	$[\bar{1}01]$	0.46	0.20	0.08	0.17
4	$(\bar{1}11)$	$[0\bar{1}1]$	0.37	0.05	0.48	0.33
5	$(\bar{1}11)$	[101]	0.03	0.04	0.30	0.28
6	$(\bar{1}11)$	[110]	0.40	0.01	0.19	0.06
7	(111)	$[0\bar{1}1]$	0.20	0.30	0.31	0.41
8	(111)	$[\bar{1}10]$	0.43	0.17	0.22	0.45
9	(111)	$[\bar{1}01]$	0.23	0.13	0.09	0.04
10	$(\bar{1}\bar{1}1)$	[011]	0.16	0.35	0.18	0.07
11	$(\bar{1}\bar{1}1)$	[101]	0.17	0.10	0.49	0.05
12	$(\bar{1}\bar{1}1)$	$[\bar{1}10]$	0.01	0.44	0.31	0.02

For single crystal SC1, the Schmid factors of slip systems 3, 6, and 8 are above 0.4, with slip system 3 having the highest Schmid factor of 0.46. Consequently, it can be confirmed that slip system 3 is activated for the single crystal SC1. Similarly,

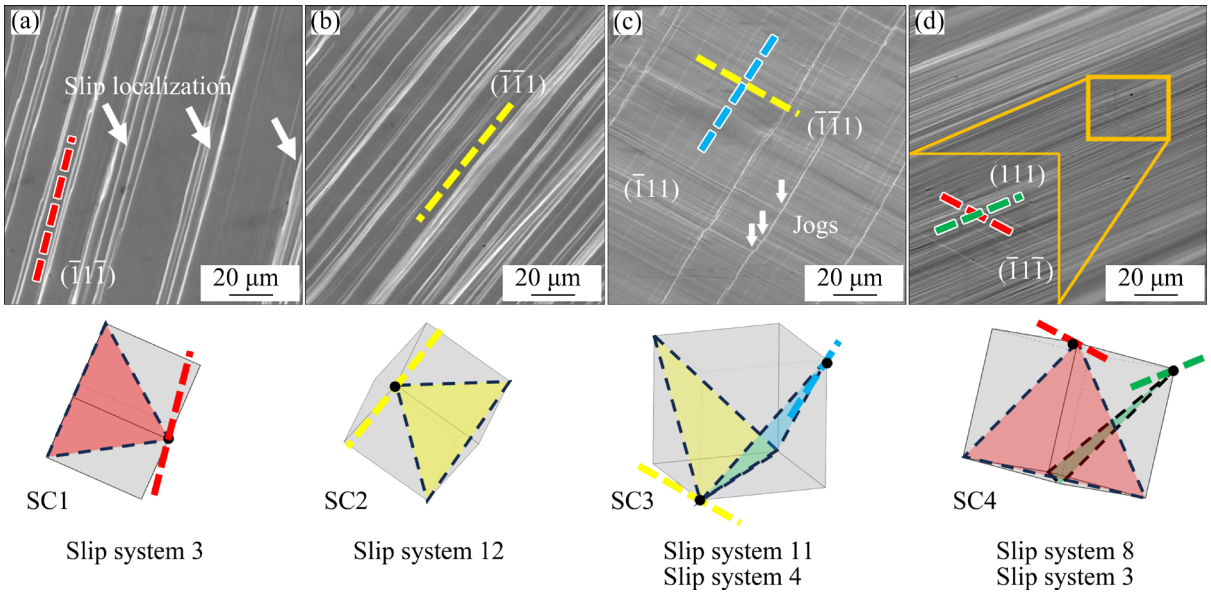

Fig. 4 Slip traces analysis of SC1 (a), SC2 (b), SC3 (c) and SC4 (d) at room temperature

utilizing the same method, it is determined that the single crystal SC2 activates slip system 12. Observation of the surface of SC3 and SC4 reveals the presence of slip traces in both directions (Figs. 4(c, d)). The order of slip activation can be inferred from the density of the two slip traces. In SC3, primary slip system 11 is predominantly activated, evidenced by dense slip traces, while slip system 4 lags in activation, with dispersive slip traces. Conversely, SC4 exhibits the activation of the secondary slip system, although the slip traces are sparse. This occurrence is typically caused by grain rotation during deformation, resulting in a change in orientation and, consequently, the Schmid factor [31,32].

To observe the evolution of slip traces during the deformation at 250 °C, periodic scanning of the same area was conducted, as shown in Fig. 5. Except for the activated slip system of SC1, other oriented grains show different slip behavior compared with that at room temperature. As shown in Fig. 5(d), the multiple slip occurs on the surface of single crystal SC2 when the strain is 5%. The dislocations initially located on the slip plane $(\bar{1}\bar{1}1)$ migrates to the other slip plane $(\bar{1}1\bar{1})$, leading to a transition from multiple slip to cross slip, as illustrated in Fig. 5(f). As can be seen from Fig. 3(b), the stress−strain curve of SC2 exhibits periodic sudden drops in stress, potentially attributed to the occurrence of cross slip [33]. The initial stress drop manifests at 9% strain, likely marking the critical point of multiple slip transition.

The width between the slip traces in the direction perpendicular to the slip traces of the main

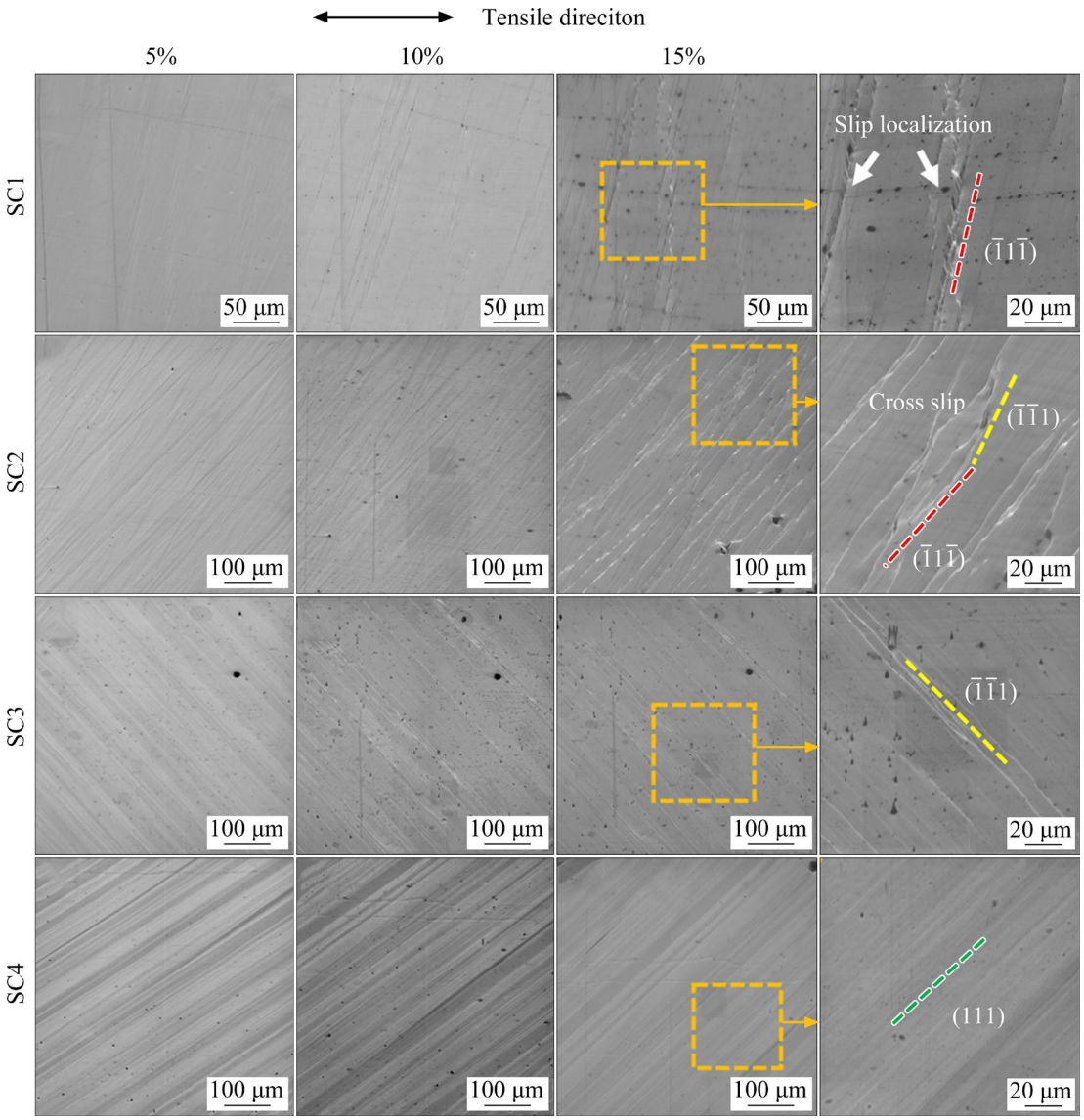

Fig. 5 Slip traces analysis of SC1 (a), SC2 (b), SC3 (c) and SC4 (d) at 250 °C

slip system is calculated to further analyze the influence of temperature on the slip behavior. The distributions of main slip traces spacing at 15% strain are shown in Fig. 6, where each point represents a slip trace, and the average width and standard deviation are calculated in Table 2.

The average slip trace spacing of SC1 is larger than that of other oriented grains at different temperatures, with the maximum distance being 2.5−6.5 times that of other grains. This indicates significant slip localization in SC1. Moreover, the minimum width increases from 0.455 at room temperature to 3.243 μm, indicating exacerbated local slip behavior at 250 °C. Such highly localized slip bands arise from the clustering of dislocations along the crystal plane and their orderly slip along a specific direction, as prominently illustrated within a confined area of the crystal [34]. However, the slip planes are uniformly distributed across SC3 and SC4 crystals with various orientations, and the closely aligned slip traces nearly overlap each other. A comparison of Figs. 6(c, d) reveals a slight decrease in the degree of slip trace spacing in the two grains, potentially attributed to the enhanced ordered long-range motion of dislocations at 250 °C, thereby reducing the number of dislocation sources

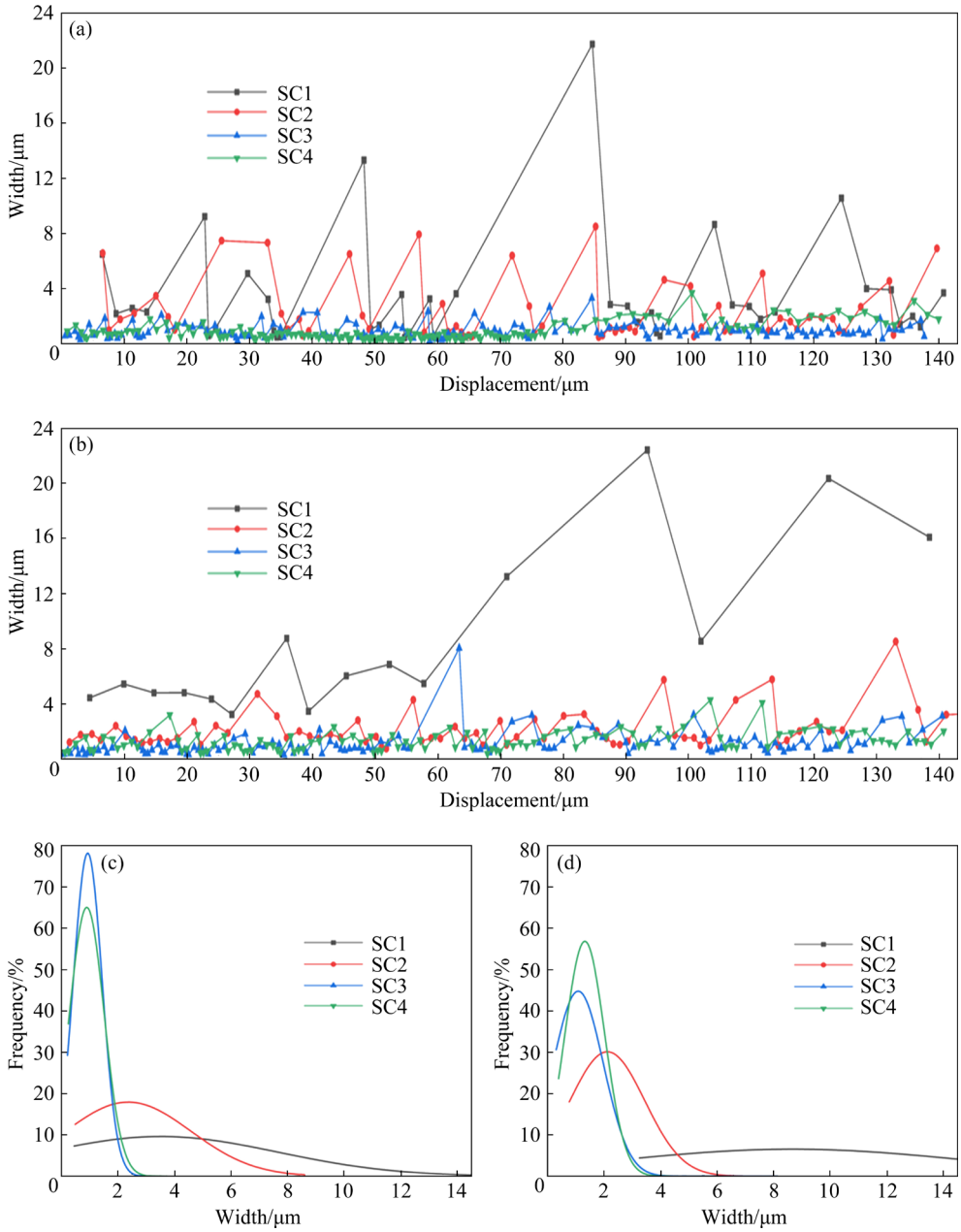

Fig. 6 Evolution (a, b) and normal distribution (c, d) of slip trace width of principal slip system at 15% strain: (a, c) At room temperature; (b, d) At 250 °C

representing slip planes [35,36]. It is noteworthy that the spacing of slip traces on SC2 at 250 °C is more concentrated compared to that at room temperature, as depicted in Figs. 6(c, d). This contributes to the transition from multiple slip to cross slip.

3.3 Oriented-precipitation of *T*1 and *θ′* phases

To analyze the influence of orientation on the precipitation behavior of the Al−Cu−Li alloy during deformation at 250 °C, the distribution of precipitates at 15% strain is observed. Figure 7 presents the high-angle annular dark-field scanning transmission electron micrographs (HAADF-STEMs) observed along the [110] zone axis. The size and volume fractions of the *T*1 and *θ′* phases are detailed in Table 3. It is evident that the *θ′* phase predominates, with only a small amount of the *T*1 phase, as depicted in Figs. 7(a−d). Upon examining the statistical data in Table 3, it becomes apparent that the diameters and thicknesses of the *T*1 and *θ′* phases in single crystals SC1, SC3, and SC4 are similar, yet distinct from those in SC2. The precipitates in SC2 are larger and thinner compared to other grains. Additionally, the volume fraction of precipitates in SC3 and SC4 is similar but lower than that in SC1 and SC2. Hence, it can be concluded that the precipitation behavior of the Al−Cu−Li alloy exhibits a degree of orientation sensitivity.

Only two of four variants of the *T*1 phase are visible under the [110] zonal axis [37]. In Figs. 7(a−d), *T*1 phases in one direction are seen predominantly. This discrepancy suggests significant differences in the proportion of *T*1 variants precipitated during high-temperature deformation with different orientations. This can be attributed to variations in the Schmidt factors of

Table 2 Average, maximum, minimum and standard deviation of slip trace width at room temperature and 250 °C

Sample	Mean width/μm		Maximum width/μm		Minimum width/μm		Standard deviation/μm	
	25 °C	250 °C	25 °C	250 °C	25 °C	250 °C	25 °C	250 °C
SC1	3.625	8.652	21.753	22.432	0.455	3.243	4.143	6.087
SC2	2.368	2.110	8.523	8.529	0.491	0.765	2.223	1.325
SC3	0.937	1.081	3.335	8.056	0.221	0.303	0.510	0.891
SC4	0.903	1.315	3.707	4.290	0.250	0.385	0.613	0.702

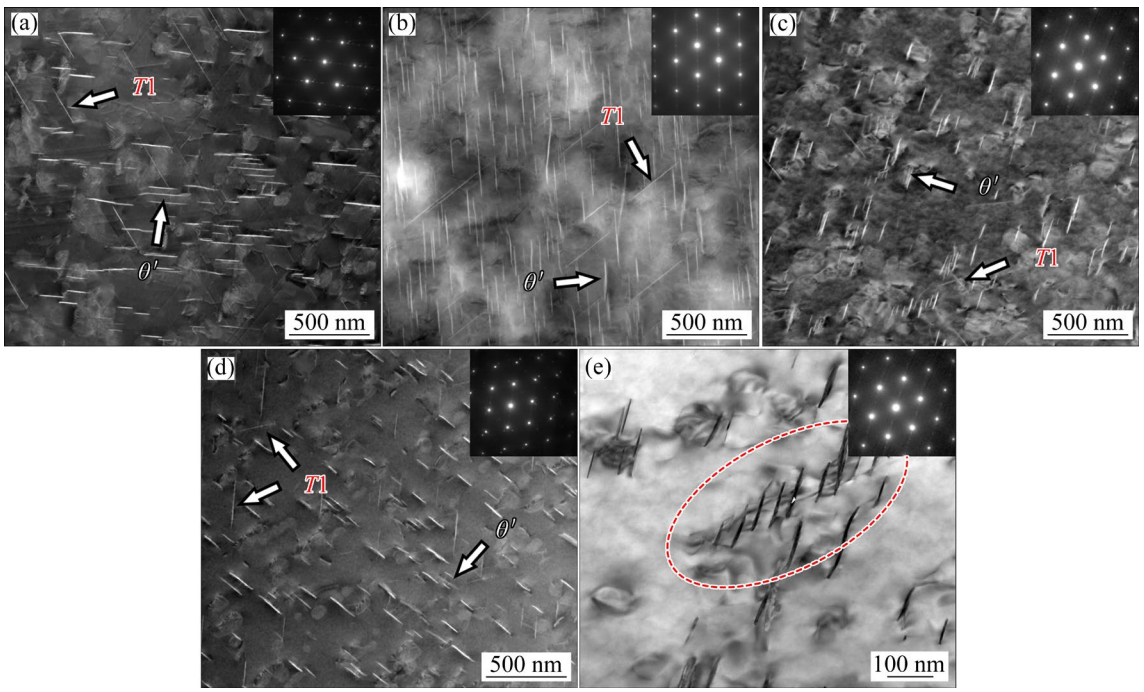

Fig. 7 HAADF-STEM images of SC1 (a), SC2 (b), SC3 (c) and SC4 (d) at 250 °C; Bright field (BF) image illustrating precipitates on dislocations (e) (The beam direction is along [110] zone axis)

different slip planes, resulting in dissimilar dislocation production, thereby influencing the precipitation of the *T*1 phase [38].

3.4 Crack initiation and propagation behavior

In this study, the crack initiation behavior of Al−Cu−Li single crystals with different orientations during the deformation at 250 °C is analyzed. The crack initiation and propagation behavior of the single crystals at 30% strain exhibits unique characteristics, as depicted in Fig. 8. Observations from Figs. 5(a−c) reveal that local slip bands on the surface of SC1 are accompanied by the initiation of microcracks.

As the loading progressed, microcracks on the slip line gradually propagated, as shown in Fig. 8(b). A significant shear step emerges on the surface of the sample, indicating proximity to fracture, as depicted in Fig. 8(a). In the vicinity of the unstable shear zone, a series of widely spaced shear bands are formed, originating from the localized slip zone, as indicated by the arrow in Fig. 8(a).

There is the close relationship between slip localization and crack nucleation [34]. At this stage, single crystal SC2 is far from its tensile limit, with no obvious cracks detected on specimen surface, as depicted in Fig. 8(c). However, following the transition from multiple slip to cross slip, a substantial concentration of slip lines occurs, leading to dislocation plugging and subsequent stress concentration. As depicted in Fig. 8(d), there is a prominent coarse slip band with significant deformation in the surrounding area, serving as the preferred location for crack nucleation and propagation. The cracks initially propagate along a single slip band in SC3. The region between the crack and the adjacent slip band experiences severe distortion, facilitating crack transfer to the neighboring slip band. Subsequently, the crack tip continues to propagate along the new slip band. There is no direct correlation between the slip trace and the initiation and propagation of cracks in SC4

Table 3 Quantitative measurements of θ' and *T*1 precipitates for four single crystals

Samlpe	*d*/nm		*t*/nm		*f*/%	
	θ'	*T*1	θ'	*T*1	θ'	*T*1
SC1	108.4±90.6	214.9±112.3	10.55±1.21	4.30±1.15	2.33	0.32
SC2	155.7±103.2	258.7±125.7	5.67±1.34	3.64±0.53	4.23	0.56
SC3	101.2±57.1	227.3±152.4	10.42±0.55	4.58±0.86	2.40	0.29
SC4	109.7±57.0	210.9±127.8	10.34±1.04	4.68±0.74	2.65	0.36

d, *t* and *f* stand for average plate diameter, average plate thickness, and volume fraction, respectively

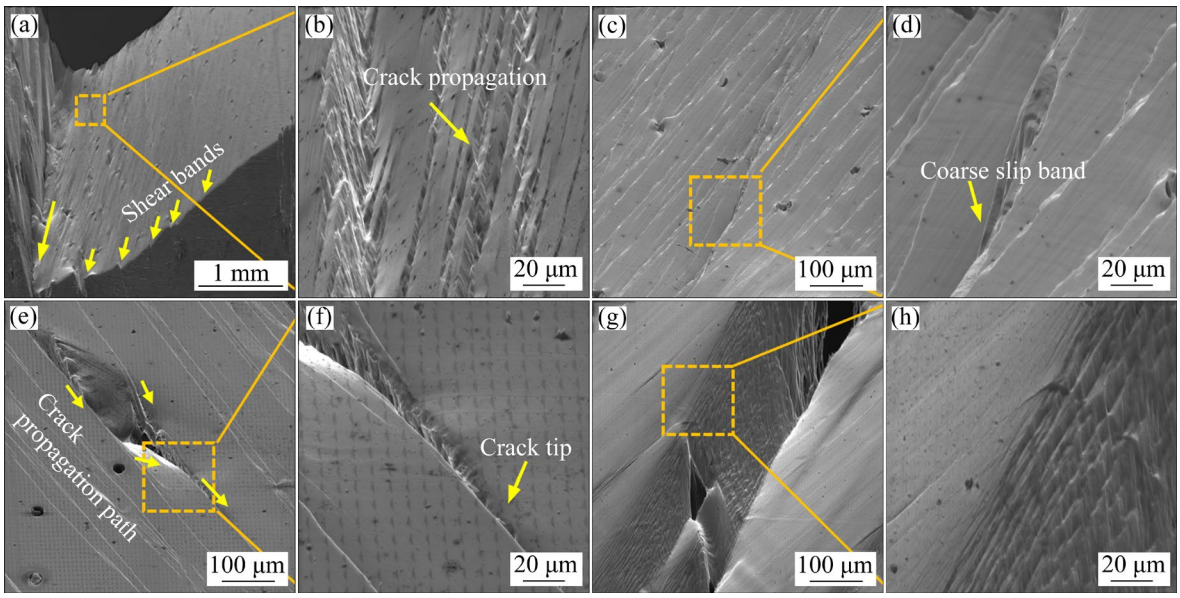

Fig. 8 SEM images of SC1 (a, b), SC2 (c, d), SC3 (e, f) and SC4 (g, h) at 250 °C

(Fig. 8(g)). In summary, the variations in slip behavior are attributable to different orientations, ultimately resulting in diverse fracture mechanisms.

4 Discussion

The yield strength of a single crystal depends on the minimum resolved shear stress required for the initiation of the slip system, and this minimum resolved shear stress is determined by crystal orientation. However, as temperature increases, the driving force for dislocation motion decreases, leading to a reduction in yield strength [39]. Therefore, the yield strength of Al−Cu−Li single crystals at 250 °C is lower than that at room temperature. Importantly, orientation dependence of the yield strength of Al−Cu−Li single crystals is significantly diminished at 250 °C (Fig. 3).

At room temperature, deformation in a single crystal is primarily determined by interactions between dislocations, defining the average distance that a dislocation travels before interacting with an obstacle for storage as the average free path length [40,41]. In grains with activated single slip, dislocation motion on parallel glide planes encounters fewer hindrances, resulting in a larger mean free path length. Conversely, in grains with activated multiple slip systems, where numerous dislocations undergo cross-slip, strong interactions between multiple slip systems occur, leading to a lower mean free path length [31,42]. As illustrated in Fig. 4(c), after the secondary slip system $(\bar{1}11)[0\bar{1}1]$ is activated, the dislocation on the main slip plane $(\bar{1}\bar{1}1)$ is cut and dragged along the slip direction of the former, forming a jog between the dragged dislocation line and the original dislocation line. The jogs impede further dislocations movement, leading to dislocations accumulation, high stress concentration, and the initiation of cleavage cracks. Hence, this mechanism may explain why the elongation of single crystal SC3 is lower compared to SC2 and SC4. However, in grains with activated single slip, once deformation localization occurs, dislocation motion is limited to a limited number of slip bands, resulting in a high amount of dislocation per slip band [43,44]. The slip localization in single crystal SC1 is more pronounced, with fewer slip bands per unit distance (Figs. 4 and 6). The convergence of numerous slip traces leads to significant strain hardening and premature failure. Conversely, the slip traces in single crystal SC2 are evenly distributed (Fig. 4(b)), allowing dislocations to spread across multiple slip planes. Consequently, there are fewer dislocations in each slip band, promoting coordinated deformation and enhanced plasticity.

As shown in Fig. 7, dislocations promote the formation of precipitates and increases the diversity of single crystal deformation mechanisms [9]. As shown in Fig. 7(e), dislocations promote the formation of precipitates and increase the diversity of single crystal deformation mechanisms. The Orowan rings and wavy dislocation cells (referred to as matrix dislocation self-trapping) [15] can be observed in Fig. 9, and they are depicted in a high-magnification image in Fig. 9(f). The cell is a long-kinked screw dislocation, which is constantly bent and eventually evolves into a corrugated structure composed of a set of tightly arranged spiral turns [45−47], as depicted in Fig. 9(e). When the distance between precipitates is large, the self-trapping mechanism between dislocations tends to replace other interactions. Conversely, the dislocation interacts with the precipitates to form an Orowan ring. Therefore, in SC1 with the lowest volume fraction of precipitates, the large spacing between precipitates leads to dislocation self-trapping, forming wide-ranging corrugated dislocation cells. This phenomenon is closely associated with the observed slip localization, as depicted in Fig. 10(a). In SC3 and SC4, the precipitates with intermediate particle spacing mediate the formation of dislocation cells and determine their size [41]. Subsequently, these tiny dislocation cells contribute to the formation of widely distributed slip bands, as shown in Fig. 10(b). This can be proven from the good elongation caused by this deformation mechanism that can prevent premature failure by inhibiting strain localization [48].

Previously, it has been observed that the deformation mechanism of SC2 at 250 °C shifts from multiple slip to cross slip. The activation of multiple slip provides more potential dislocation sources and facilitates dynamic precipitation [44], which also accounts for the higher volume fraction of precipitates in SC2. Additionally, the diameters of the θ' and $T1$ phases in SC2 are larger than in other grains, further reducing the particle spacing, as indicated in Table 3. As a consequence, there are

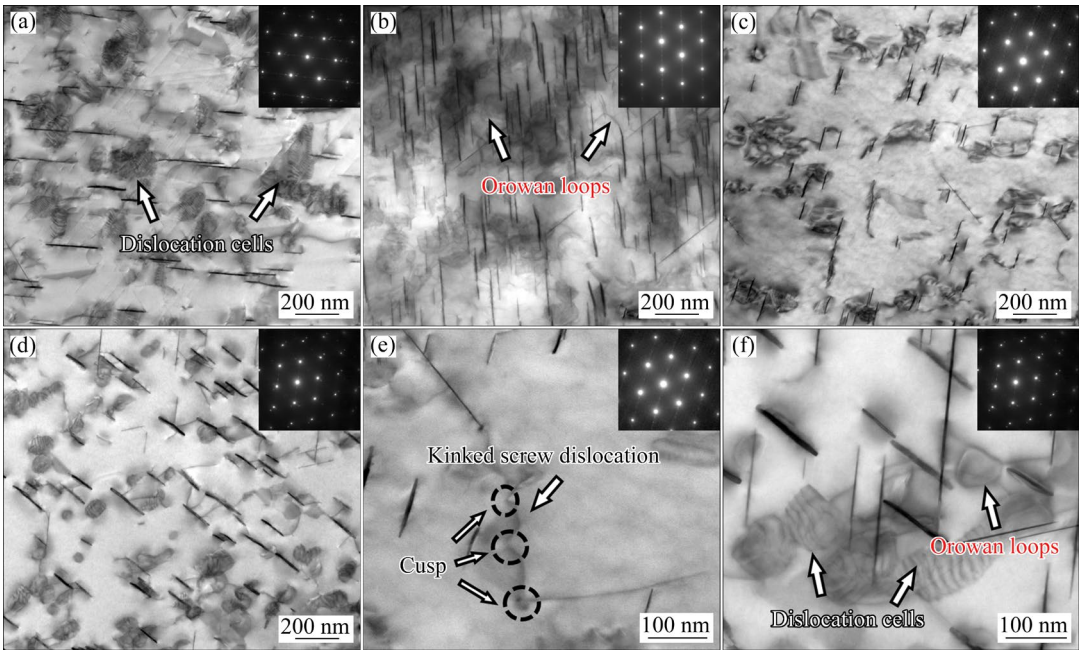

Fig. 9 BF images of SC1 (a), SC2 (b), SC3 (c) and SC4 (d) under 15% strain at 250 °C; BF image showing structure of kinked screw dislocation (e); BF image displaying dislocation self-trapping and Orowan mechanism (f) (The beam direction is along [110] zone axis)

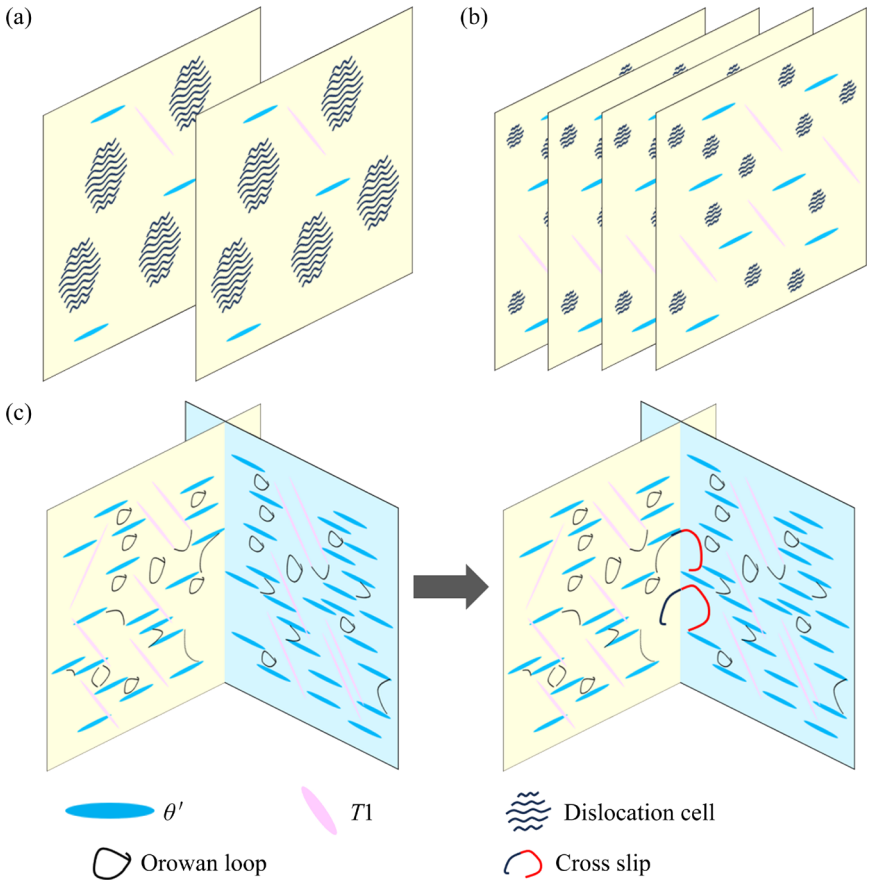

Fig. 10 Deformation mechanisms of single crystals with varying orientations at 250 °C: (a) Large dislocation cells formed on localized slip bands in single crystal SC1; (b) Small dislocation cells developing on extensive slip bands in single crystals SC3 and SC4; (c) Cross slip of dislocations occurring onto another slip plane in single crystal SC2, where Orowan rings dominate

fewer dislocation cells in SC2, and the Orowan rings have a dominant role in controlling the deformation (Fig. 9(b)). Clearly, the stress concentration caused by the small Orowan ring structure is much smaller than that induced by the large dislocation cell structure. Consequently, the strength of SC2 in the early stage is lower than that of other grains. It has been demonstrated that the movement of dislocation between cross slip bands is unhindered [48]. Therefore, following the transition from multiple slip to cross slip, the free path length of dislocation increases, effectively averting premature material failure caused by dislocation plugging, as illustrated in Fig. 10(c). Consequently, the ductility of single crystal SC2 at 250 °C surpasses that of other oriented grains. Subsequently, as deformation progresses, dislocation proliferation and precipitation continue to occur, causing the strength of SC2 to gradually increase until fracture. In summary, variations in crystal orientations lead to changes in the distribution of precipitates and alterations in deformation mechanisms, ultimately resulting in differences in final performance.

5 Conclusions

(1) The yield strength of Al−Cu−Li single crystals is influenced by both crystal orientation and temperature. The maximum yield strength difference between single crystals with different orientations decreases from 41.6% at room temperature to 20.1% at 250 °C.

(2) Slip behavior is one of the important factors that lead to the great difference of ductility of single crystals among these orientations. At room temperature, the maximum difference of elongation between single crystals is 14.7%. For SC1, the localized slip behavior shows the accumulation of severe dislocations on specific slip planes, in which cracks are generated at early deformation stage, thereby reducing ductility. Conversely, the homogeneous distribution of slip planes and activation of multiple slip systems contribute to enhanced ductility.

(3) During tensile deformation, the distribution of dislocations is also influenced by crystal orientation, consequently affecting the size and volume fraction of precipitates in different Al−Cu−Li single crystals. The total number of precipitates in SC2 is 1.6−1.8 times that of other grains at 15% strain.

(4) Compared to that at room temperature, the maximum difference in elongation among all selected grains increases to 20.8% at 250 °C. SC1, characterized by minimal precipitated phases, primarily undergoes dislocation self-trapping, leading to enhanced slip localization and a substantial decrease in ductility. On the other hand, SC2, which contains the most precipitates, predominantly operates via the Orowan mechanism. This activation of multiple slip systems evolves into cross slip characteristics, significantly enhancing the plastic deformation capacity of the Al−Cu−Li alloy.

CRediT authorship contribution statement

Zhen JIANG: Data acquisition, Writing – Original draft; **Chen-qi LEI:** Supervision; **Jia-jun DING:** Data acquisition; **Chun-nan ZHU:** Conceptualization, Formal analysis; **Dong-feng SHI:** Investigation, Validation, Supervision; **Jin ZHANG:** Conceptualization, Funding acquisition; **Guo-qing WANG:** Supervision, Funding acquisition.

Declaration of competing interest

The authors declare that they have no known competing financial interests or personal relationships that could have appeared to influence the work reported in this paper.

Acknowledgments

This work was supported by the National Natural Science Foundation of China (No. U21B6004), Major Project of Scientific Innovation of Hunan Province, China (No. 2021GK1040), and National Key R&D Program of China (No. 2020YFA0711104).

References

[1] WANG Cheng, ZHANG Jin. Effect of pretreatment on precipitation of Al_3Zr dispersoids and recrystallization behavior of spray deposited Al−Cu−Li alloy [J]. Journal of Central South University, 2023, 30(2): 365−373.

[2] LIN Ben, MA Peng-cheng, LI Hao-ran, DENG San-xi, ZENG Guang-jun, TANG Jian-guo, LI Jin-feng, LI Xi-wu. Anisotropy of Al−Li alloy plate and its heredity effect in mechanical property distribution of spun-dome [J]. Transactions of Nonferrous Metals Society of China, 2023, 33(5): 1318−1330.

[3] YANG Sheng-li, LIU Le-le, GAO Fu-yang, Xu Zhe, SONG

De-jun, JIANG Peng. Evolution of texture and precipitates in Al−Cu−Li alloy during deformation and heat treatment and its effect on anisotropy [J]. Materials Research Express, 2021, 8(5): 056509.

[4] HOSFORD W F, ZEISLOFT R H. The anisotropy of age-hardened Al-4 pct Cu single crystals during plane-strain compression [J]. Metallurgical Transactions, 1972, 3(1): 113−121.

[5] GHORBANHOSSEINI S, FERESHTEH-SANIEE F, SONBOLI A. An experimental investigation on the influence of elevated-temperature constrained groove pressing on the microstructure, mechanical properties, anisotropy and texture of 2024 Al sheets [J]. Journal of Alloys and Compounds, 2020, 817: 152763.

[6] NAYAN N, MISHRA S, PRAKASH A, MURTY S, PRASAD M, SAMAJDAR I. Effect of cross-rolling on microstructure and texture evolution and tensile behavior of aluminium-copper-lithium (AA2195) alloy [J]. Materials Science and Engineering A, 2019, 740: 252−261.

[7] ZHAO Xin-yue, LIU Wen-sheng, XIAO Dai-hong, MA Yun-zhu, HUANG Lan-ping, TANG Ya. A critical review: Crystal structure, evolution and interaction mechanism with dislocations of nano precipitates in Al−Li alloys [J]. Materials & Design, 2022, 217: 110629.

[8] MURAYAMA M, HONO K. Role of Ag and Mg on precipitation of *T*1 phase in an Al−Cu−Li−Mg−Ag alloy [J]. Scripta Materialia, 2001, 44: 701−706.

[9] GABLE B M, ZHU A W, CSONTOS A A, STARKE E A. The role of plastic deformation on the competitive microstructural evolution and mechanical properties of a novel Al−Li−Cu−X alloy [J]. Journal of Light Metals, 2001, 1(1): 1−14.

[10] KIM N J, LEE E W. Effect of *T*1 precipitate on the anisotropy of Al□Li alloy 2090 [J]. Acta Metallurgica et Materialia, 1993, 41(3): 941−948.

[11] ES-SAID O S, PARRISH C J, BRADBERRY C A, HASSOUN J Y, PARISH R A, NASH A, SMYTHE N C, TRAN K N, RUPERTO T, LEE E W, MITCHELL D, VINQUIST C. Effect of stretch orientation and rolling orientation on the mechanical properties of 2195 Al−Cu−Li alloy [J]. Journal of Materials Engineering and Performance, 2010, 20(7): 1171−1179.

[12] LI Yao, XU Guo-fu, QIAO Hai-guang, LIU Shi-chao, PENG Xiao-yan. Effect of pre-deformation on microstructure and mechanical properties of 2050 Al−Li alloy [J]. Transactions of Nonferrous Metals Society of China, 2024, 34(6): 1774−1788.

[13] MISHRA S, YADAVA M, KULKARNI K N, GURAO N P. A theoretical investigation of the effect of precipitate habit plane on plastic anisotropy in age hardenable aluminium alloys [J]. Modelling and Simulation in Materials Science and Engineering, 2018, 26(5): 055011.

[14] MEDJAHED A, MOULA H, ZEGAOUI A, DERRADJI M, HENNICHE A, WU R Z, HOU L G, ZHANG J H, ZHANG M L. Influence of the rolling direction on the microstructure, mechanical, anisotropy and gamma rays shielding properties of an Al−Cu−Li−Mg−X alloy [J]. Materials Science & Engineering A, 2018, 732: 129−137.

[15] MILLIGAN B, MA D, ALLARD L, CLARKE A, SHYAM A. Crystallographic orientation-dependent strain hardening in a precipitation-strengthened Al−Cu alloy [J]. Acta Materialia, 2021, 205: 116577.

[16] JIANG Zhen, ZHANG Jin, SHI Dong-feng, LEI Chen-qi. Quasi-in-situ EBSD study on the influence of precipitations on the strength, plasticity and deformation mechanism in Al−Cu−Li alloys [J]. Metals and Materials International, 2024, 30(7): 1895−1909.

[17] ZHAO Tian-zhang, JIN Long, XU Yong, ZHANG Shi-hong. Anisotropic yielding stress of 2198 Al−Li alloy sheet and mechanisms [J]. Materials Science and Engineering A, 2020, 771: 138572.

[18] SMITH J, LIU W K, CAO J. A general anisotropic yield criterion for pressure-dependent materials [J]. International Journal of Plasticity, 2015, 75: 2−21.

[19] LIU Mao, TIEU A K, PENG C T, ZHOU Kun. Explore the anisotropic indentation pile-up patterns of single-crystal coppers by crystal plasticity finite element modelling [J]. Materials Letters, 2015, 161: 227−230.

[20] LIU Mao, WANG Peng-fei, LU Guo-xing, HUANG Cheng-yao, YOU Zhong, WANG Chien-he, YEN Hung-wei. Deformation-activated recrystallization twin: New twinning path in pure aluminum enabled by cryogenic and rapid compression [J]. iScience, 2022, 25(5): 104248.

[21] SHI Dong-feng, MA A, PÉREZ-PRADO M T, CEPEDA-JIMÉNEZ C M. Activation of second-order ⟨*c*+*a*⟩ pyramidal slip and other secondary mechanisms in solid solution Mg−Zn alloys and their effect on tensile ductility [J]. Acta Materialia, 2023, 244: 118555.

[22] YANG Biao-biao, SHI Chen-ying, LAI Rui-lin, SHI Dong-feng, GUAN Di-kai, ZHU Gao-ming, CUI Yu-jie, XIE Guo-qiang, LI Yun-ping, CHIBA A, LLORCA J. Identification of active slip systems in polycrystals by slip trace-modified lattice rotation analysis (ST-MLRA) [J]. Scripta Materialia, 2022, 214: 114648.

[23] YE Zhen-hua, LI Chuan-wei, ZHENG Meng-yao, ZHANG Xin-yu, YANG Xu-dong, GU Jian-feng. In situ EBSD/DIC-based investigation of deformation and fracture mechanism in FCC- and L12-structured FeCoNiV high-entropy alloys [J]. International Journal of Plasticity, 2022, 152: 103247.

[24] FURUKAWA M, HORITA Z, LANGDON T G. Principles of deformation in single crystals of two different orientations processed by equal-channel angular pressing [J]. Materials Science and Engineering A, 2009, 503: 21−27.

[25] GUO Yi-zhong, TENG Jiao, YANG Guo, LI Ang, DENG Yao, YANG Cheng-peng, WANG Li-hua, YAN Xin, ZHANG Ze, LI Xiao-yan, MA En, HAN Xiao-dong. In situ observation of atomic-scale processes accomplishing grain rotation at mixed grain boundaries [J]. Acta Materialia, 2022, 241: 118386.

[26] LINNE M A, BIELER T R, DALY S. The effect of microstructure on the relationship between grain boundary sliding and slip transmission in high purity aluminum [J].

International Journal of Plasticity, 2020, 135: 102818.

[27] LI Hao-ran, ZOU Zhi-tao, LI Jin-feng, XU Guo-fu, ZHENG Zi-qiao. Correlation between grain structures and tensile properties of Al−Li alloys [J]. Transactions of Nonferrous Metals Society of China, 2023, 33(12): 3597−3611.

[28] JIN N Y, WINTER A T. Cyclic deformation of copper single crystals oriented for double slip [J]. Acta Metallurgica, 1984, 32(7): 989−995.

[29] LI X W, WANG Z G, LI S X. Influence of crystallographic orientation on cyclic strain-hardening behaviour of copper single crystals [J]. Philosophical Magazine Letters, 1999, 79(11): 869−875.

[30] NAKANO T, OMOMOTO Y, HAGIHARA K, UMAKOSHI Y. Plastic deformation behavior and operative slip systems of ZrSi2 single crystals with C49 type of structure [J]. Scripta Materialia, 2003, 48: 1307−1312.

[31] SCHILLI S, SEIFERT T, KREINS M, KRUPP U. Bauschinger effect and latent hardening under cyclic micro-bending of Ni-base Alloy 718 single crystals: Part II. Single crystal plasticity modeling with latent kinematic hardening [J]. Materials Science and Engineering A, 2022, 830: 142030.

[32] CAI M D, LANGFORD S C, DICKINSON J T. Orientation dependence of slip band formation in single-crystal aluminum studied by photoelectron emission [J]. Acta Materialia, 2008, 56: 5938−5945.

[33] HUSSEIN A M, RAO S I, UCHIC M D, DIMIDUK D M, EL-AWADY J A. Microstructurally based cross-slip mechanisms and their effects on dislocation microstructure evolution in fcc crystals [J]. Acta Materialia, 2015, 85: 180−190.

[34] STINVILLE J C, CHARPAGNE M A, CERVELLON A, HEMERY S, WANG F, CALLAHAN P G, VALLE V, POLLOCK T M. On the origins of fatigue strength in crystalline metallic materials [J]. Science, 2022, 377(6610): 1065−1071.

[35] WELSCH E, PONGE D, HAGHIGHAT S M H, SANDLÖBES S, CHOI P, HERBIG M, ZAEFFERER S, RAABE D. Strain hardening by dynamic slip band refinement in a high-Mn lightweight steel [J]. Acta Materialia, 2016, 116: 188−199.

[36] KIENER D, MOTZ C, GROSINGER W, WEYGAND D, PIPPAN R. Cyclic response of copper single crystal micro-beams [J]. Scripta Materialia, 2010, 63: 500−503.

[37] HU Wei, CHEN Ji-qiang, HAN Shuang, XU Jin-jun, MIAO Jia-le, XING Ting, GUAN Ren-guo. Initial report on the oriented-precipitation of *T*1-phase in creep-aged Al−Cu−Li single crystal [J]. Metals and Materials International, 2023, 29(5): 1382−1389.

[38] ZHAO Tian-zhang, FAN Zhi-xian, XIE Hong-zhi, CHEN Hong-ran, CHEN Shuai-feng, ZHANG Shi-hong. A new modeling framework for anisotropic yield strength of Al−Li alloy sheet with inhomogeneous plate-like *T*1 precipitates [J]. International Journal of Plasticity, 2022, 157: 103396.

[39] PAIK S, NAVEEN KUMAR N, DUTTA B K, TEWARI R, DURGAPRASAD P V. Experimental investigation and crystal plasticity simulation with damage for single crystal copper subjected to tensile load [J]. Metals and Materials International, 2023, 29(3): 618−633.

[40] DEVINCRE B, HOC T, KUBIN L. Dislocation mean free paths and strain hardening of crystals [J]. Science, 2008, 320(5884): 1745−1748.

[41] KAIRA C S, KANTZOS C, WILLIAMS J J, DE ANDRADE V, de CARLO F, CHAWLA N. Microstructural evolution and deformation behavior of Al−Cu alloys: A Transmission X-ray Microscopy (TXM) and micropillar compression study [J]. Acta Materialia, 2018, 144: 419−431.

[42] DING Qing-qing, ZHANG Yin, CHEN Xiao, FU Xiao-qian, CHEN Deng-ke, CHEN Si-jing, GU Lin, WEI Fei, BEI Hong-bin, GAO Yan-fei, WEN Min-ru, LI Ji-xue, ZHANG Ze, ZHU Ting, RITCHIE R O, YU Qian. Tuning element distribution, structure and properties by composition in high-entropy alloys [J]. Nature, 2019, 574(7777): 223−227.

[43] VELAYARCE J R, ZAMANZADE M, ABAD O T, MOTZ C. Influence of single and multiple slip conditions and temperature on the size effect in micro bending [J]. Acta Materialia, 2018, 154: 325−333.

[44] HA J S, HONG S I. Temperature dependent slip mode modification in Cu−Al solid solution alloy single crystals [J]. Materials Science and Engineering A, 2013, 565: 9−12.

[45] RAJINIKANTH V, JINDAL V, AKKIMARDI V G, GHOSH M, VENKATESWARLU K. Transmission electron microscopy studies on the effect of strain on Al and Al−1%Sc alloy [J]. Scripta Materialia, 2007, 57: 425−428.

[46] JIAO Ben-qi, ZHAO Qin-yang, ZHAO Yong-qing, ZHANG Wen, LI Yan-chao, HU Zhong-wu, GAO Xuan-qiao, CUI Chang-xing, XIN Tian. Impact characteristic and crack propagation mechanisms of large-size molybdenum alloy single crystal and polycrystal [J]. International Journal of Refractory Metals & Hard Materials, 2022, 107: 105871.

[47] MILLIGAN B, MA D, ALLARD L, CLARKE A, SHYAM A. Dislocation-θ'(Al2Cu) interactions during creep deformation of an Al−Cu alloy [J]. Scripta Materialia, 2022, 217: 114739.

[48] KIM S D, PARK J Y, PARK S J, JANG J H, MOON J, HA H Y, LEE C H, KANG J Y, SHIN J H, LEE T H. Direct observation of dislocation plasticity in high-Mn lightweight steel by in-situ TEM [J]. Scientific Reports, 2019, 9: 15171.

取向和温度对 Al−Cu−Li 单晶滑移行为和析出行为的协同效应

蒋 震[1]，雷郴祁[1]，丁佳俊[1]，祝春楠[1]，石东风[1,2]，张 劲[1,2]，王国庆[3]

1. 中南大学 轻合金研究院，长沙 410083；
2. 中南大学 高性能与复杂制造国家重点实验室，长沙 410083；
3. 中国运载火箭技术研究院，北京 100076

摘 要：利用电子背散射衍射(EBSD)和透射电子显微镜(TEM)研究了 4 种不同取向的 Al−Cu−Li 单晶在不同温度下的滑移行为和析出行为。单晶在室温下的屈服强度和伸长率的最大差异分别为 41.6%和 14.7%，说明力学性能与晶体取向有很强的相关性。不同取向的单晶表现出独特的滑移特征，包括滑移均匀化、滑移局部化和多系滑移。对于单晶 SC1 来说，滑移局部化是导致其伸长率低于其他单晶的主要原因。然而，在 250 ℃变形时，不同取向单晶的析出相形貌和分布存在明显差异，导致最大伸长率差异增加到 20.8%。值得注意的是，与室温相比，析出相体积分数为 2.65%的单晶 SC1 表现出更严重的滑移局部化，而析出相体积分数为 4.79%的单晶 SC2 表现出交滑移特征，显著增强了 Al−Cu−Li 合金的塑性变形能力。

关键词：Al−Cu−Li 合金；单晶；滑移行为；取向析出；变形机制

(Edited by Bing YANG)